PAPER

Check for updates

Flaky nano-crystalline SnSe₂ thin films for photoelectrochemical current generation†

Xiuyuan Shao, ‡*a Shisheng Li ‡*abc and Dai-Ming Tang c

We report chemical vapor deposition (CVD) and photoelectrochemical properties of large-area thin films of nano-crystalline SnSe₂ on conducting FTO glass. We show that densely packed, randomly oriented SnSe₂ nanoflakes can be grown by reacting vapors of tin monoselenide (SnSe) and selenium at 550 °C without compromising the electrical properties of FTO. We demonstrate that SnSe₂/FTO is photoelectrochemically active in visible to near-UV wavelengths (350–700 nm) and exhibits incident-photon-to-current-efficiency (IPCE) as high as 3.7% at 0 V *versus* the Ag/AgCl/1 M KCl reference electrode under 350 nm light illumination.

Introduction

Photoelectrochemical cells (PECs) convert solar energy into electrical power by photo-induced electrochemical reactions at semiconductor–electrolyte interfaces.[1–3] Layered chalcogenide materials (LCMs) such as MoS₂ and WSe₂ have been considered as ideal materials for photoelectrochemical devices for a long time due to the formation of an electrocatalytically active interface with the electrolytes.[4–7] PECs with promising performance have been demonstrated with bulk crystals and thin films of a variety of LCMs.[8–12]

Recent surges of interests in this class of materials have led to remarkable advances in the optoelectronics of ultrathin LCM sheets.[13,14] Monolayer sheets of group VI transition metal dichalcogenides have been extensively studied due to their direct band gap and wide-range light-absorption properties.[15] The strong light–matter interaction and their extremely large surface-to-volume ratio make them attractive for applications in photocatalysis and photoelectrochemical applications.[16] In order to translate these attractive properties of LCMs into cell performance, it is essential to fabricate a film consisting of high-quality flakes and high surface area. Liquid exfoliation[17–20] and solvothermal synthesis[21,22] of LCMs hold promise for large-scale production, however these methods have been found to lead to many defects and a small crystal size. Crystal edges and

surface defects are considered to be recombination centers for excitons and thus, large crystal domains with low defect density are needed for PEC applications. Recent studies show that monolayer MoS₂ flakes prepared by chemical exfoliation[21] and SnSe₂ flakes synthesized by solvothermal method[22] exhibit low incident-photon-to-current-efficiency (IPCE) of ∼1%, most likely due to the limited crystal quality and the limited effective surface area. Thus, a method to fabricate large-area thin films with high surface area needs to be developed. Towards this end, chemical vapor deposition (CVD) offers a simple, controllable and scalable route to produce high-quality 2D crystals with desired morphologies.

Tin diselenide (SnSe₂) is an earth-abundant layered dichalcogenide and a promising candidate as the photoanode of PECs due to its suitable band gap (indirect bandgap ∼1 eV, and direct bandgap ∼1.5 eV at 300 K).[23] In contrast to other LCMs, CVD-grown nanostructured SnSe₂ has rarely been explored, impeding extensive explorations of PECs based on this material. Here, we present a facile low-temperature CVD growth of centimeter-scale thin films consisting of randomly oriented SnSe₂ nanoflakes on FTO glass. We show that the as-grown SnSe₂ thin film on FTO glass can be used as a photoanode for PECs. The SnSe₂/FTO electrodes exhibit excellent IPCE values as high as 3.7% conducted at 0 V potential against Ag/AgCl/1 M KCl reference electrode, significantly higher than the reported values for chemically prepared nanosheets of MoS₂ and SnSe₂.[20,21]

Fig. 1a shows the configuration of our CVD set up. Similar to the previous study,[24] selenium source was placed in the low-temperature upstream region and tin monoselenide (SnSe) powder was placed at the center of the furnace to generate SnSe vapor. A cleaned FTO glass was loaded in the low-temperature downstream (∼300–350 °C) of the quartz tube. Growth was conducted at 550 °C and in ∼1 torr Argon atmosphere. After the growth, a semitransparent gray film was deposited on the FTO

aDepartment of Physics, National University of Singapore, 6 Science Drive 2, 117546, Singapore. E-mail: xiuyuan_shao@u.nus.edu

bCentre for Advanced 2D Materials, National University of Singapore, 2 Science Drive 3, 117542, Singapore

cInternational Center for Materials Nanoarchitectonics (MANA), National Institute for Materials Science (NIMS), Namiki 1-1, Tsukuba, Ibaraki, 305-0044, Japan. E-mail: LI. Shisheng@nims.go.jp

† Electronic supplementary information (ESI) available. See DOI: 10.1039/c8ra04639e

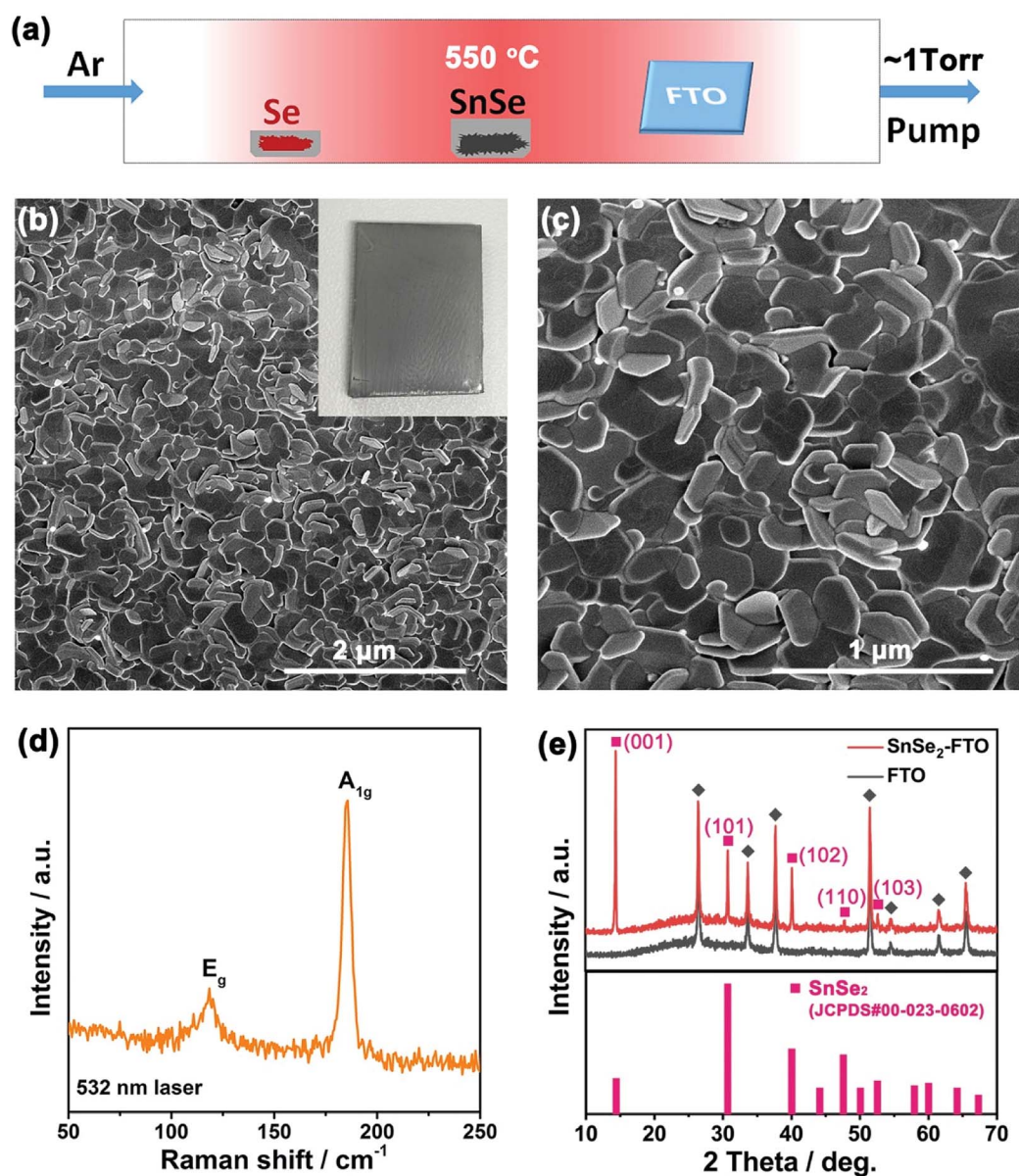‡ X. Shao and S. Li contribute equally to this work.

Fig. 1 (a) Schematic illustration of the growth set up. (b and c) SEM images of as-grown SnSe$_2$ nanoflakes on FTO glass. Inset of (b) is an optical image of SnSe$_2$/FTO glass. (d) Raman spectrum of as-grown SnSe$_2$ nanoflakes with 532 nm excitation laser. (e) XRD patterns for SnSe$_2$/FTO glass and bare FTO glass. Bottom trace represents the powder diffraction patterns for SnSe$_2$ standard.

glass (inset of Fig. 1b). The film is typically uniform across the $\sim$1.5 $\times$ 2.0 cm^2 FTO glass. Four-probe test indicates that the surface resistance of FTO-coated glass increased from $\sim$25 ohms (Ω) to $\sim$180 Ω after the growth of SnSe$_2$. The high surface conductivity of SnSe$_2$/FTO comes from the high electron mobility of SnSe$_2$ and the robust bonding between SnSe$_2$ nanoflakes and FTO glass (ESI Fig. S1†). It should be noted that the deposited SnSe$_2$ film is mostly a reaction product of Se and SnSe rather than the selenization of FTO. The combination of high electrical conductivity and the optical bandgap of $\sim$1.64 eV make the flaky SnSe$_2$ ideal for PECs (ESI Fig. S2†).

Fig. 1b and c are scanning electron microscopy (SEM) images of as-grown SnSe$_2$ nanoflakes on FTO glass. The SnSe$_2$ nanoflakes have a uniform coverage on the FTO glass. The magnified image demonstrates the as-grown SnSe$_2$ nanoflakes have a hexagonal shape with a lateral size from several tens to several hundred nanometers. This was also verified by the transmission electron microscopy (TEM) as demonstrated in Fig. 2a. The thickness of these SnSe$_2$ nanoflakes is 38.1 $\pm$ 13.7 nm. All the as-grown SnSe$_2$ nanoflakes are tilted and well bonded to the FTO glass, forming a porous 3D nanostructure (ESI Fig. S2†). The tilted and porous structure of SnSe$_2$ nanoflakes and their robust connection to the FTO glass provide high-speed channels for both ion diffusion and electron transportation, which make SnSe$_2$/FTO a good candidate for applications of PECs.[25]
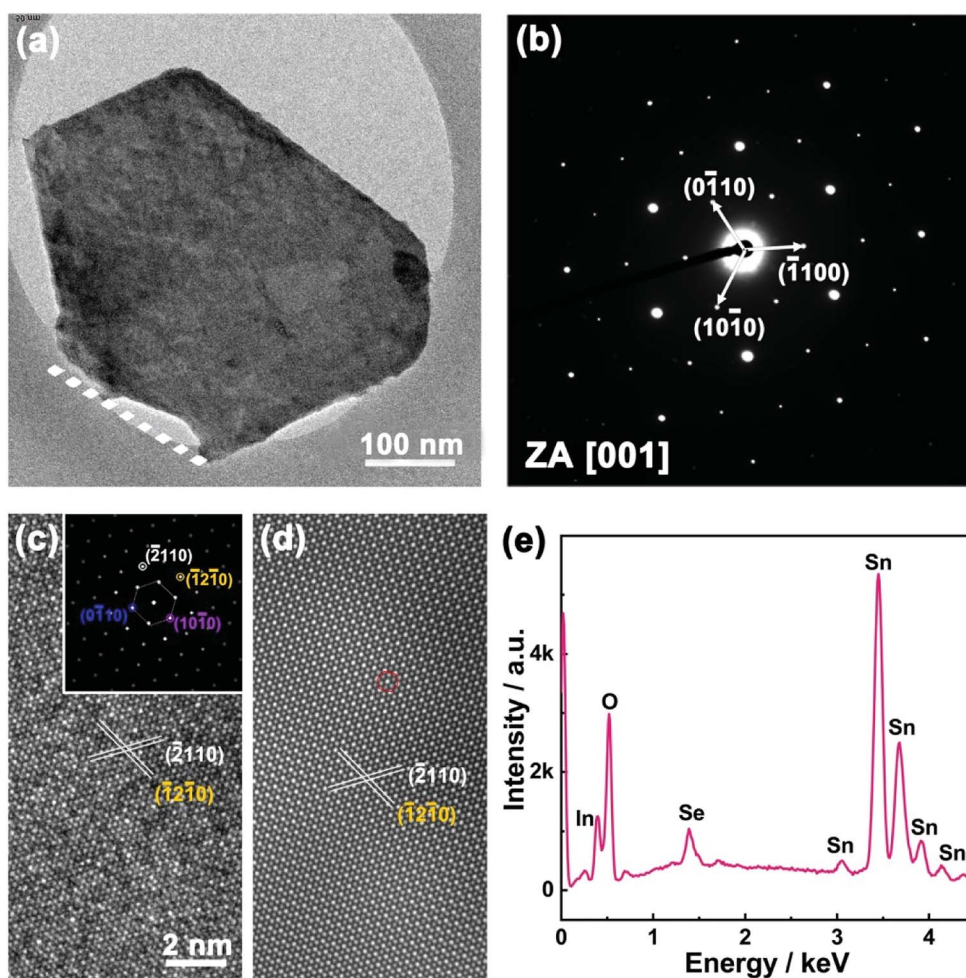
Fig. 2 (a) TEM image of a $SnSe_2$ nanoflake. (b) SAED pattern of the $SnSe_2$ nanoflake. (c) High-resolution TEM image of the $SnSe_2$ nanoflake. Inset is the corresponding fast Fourier transform (FFT) from the TEM image along [001] zone axis. (d) Inverse FFT image of the $SnSe_2$ nanoflake. (e) EDX spectrum of a $SnSe_2$ nanoflake grown on FTO glass.

Fig. 1d shows a representative unpolarized Raman spectrum of the as-grown $SnSe_2$ nanoflakes on FTO glass. Two strong peaks located at 118.3 cm^{-1} and 185.6 cm^{-1} are assigned to E_g (in-plane) and A_{1g} (out-plane) Raman active modes, respectively.[3–5] Fig. 1e shows the X-ray diffraction (XRD) patterns for $SnSe_2$/FTO and FTO glass. After the deposition of $SnSe_2$ nanoflakes on FTO glass, there are five new peaks located at 14.40°, 30.71°, 40.08°, 47.60°, 52.61° and 42.15° that can be observed. These five peaks can be assigned to the (001), (101), (102), (110) and (103) crystal planes of hexagonal $SnSe_2$ (JCPDS. no. 00-023-0602), respectively. The predominant (001) peak of $SnSe_2$ is attributed to the preferential growth along the (001) basal plane of $SnSe_2$ nanoflakes.

The quality of as-grown 2D $SnSe_2$ nanoflakes has been further examined by the selected area electron diffraction (SAED), the high-resolution TEM imaging and the energy dispersive X-ray spectroscopy (EDX). For TEM characterization, the as-grown $SnSe_2$ nanoflakes were scratched from the FTO glass. We found the $SnSe_2$ nanoflakes cannot be removed from the FTO glass even by high power ultra-sonication, revealing the

strong bonding between $SnSe_2$ nanoflakes and the FTO substrates. Fig. 2a is a TEM image of one isolated $SnSe_2$ nanoflake on a TEM grid. The as-grown $SnSe_2$ nanoflakes have a hexagonal shape with a lateral size of several hundred nanometers. Only one side of the $SnSe_2$ nanoflakes (dashed line in Fig. 2a) is bonded with FTO glass. Fig. 2b is the SAED pattern of the $SnSe_2$ nanoflake, which signifies its single-crystalline nature with an in-plane lattice constant of $a = b = 0.38$ nm, which is consistent with previous results of bulk $SnSe_2$.[24–26] The hexagonally symmetric SAED pattern is in excellent agreement with the hexagonal crystal structure of $SnSe_2$ nanoflakes ($P3m1$), and the zone axis is assigned to the [001] direction. The high-resolution TEM image and its corresponding fast Fourier transform (FFT) of the $SnSe_2$ nanoflake are demonstrated in Fig. 2c and inset, respectively. The $SnSe_2$ nanoflake with an interplanar spacing of 0.19 nm was indexed to the (−2110) planes. Fig. 2d is the inverse FFT of $SnSe_2$ nanoflakes based on the inset FFT pattern in Fig. 2c. It reveals more clearly the atomic arrangement of Sn and Se elements in the hexagonal crystal structure. In the inverse FFT image the bright dots

indicated by the red circle represent Sn atoms due to its high atomic number, while the dark dots represent Se atoms. EDX spectrum and mapping further confirm the elemental uniformity over the whole nanoflakes (Fig. 2e, ESI Fig. S3 and S4†).

As a proof-of-concept application, the SnSe$_2$/FTO electrode was assembled into a PEC as illustrated in ESI Fig. S5† and depicted in experimental section with more details. Fig. 3a shows the linear sweep voltammograms of SnSe$_2$/FTO electrode, where the black and red curves represent the current density under the "OFF" state (constant dark environment) and the "ON" state (under constant white light illumination), respectively. The linear sweep voltammograms of the bare FTO glass was conducted to confirm the magnitude of photocurrent and to exclude the contribution from the FTO substrate (ESI Fig. S6†). The corresponding switched ON/OFF photocurrent at 0 V applied potential across the cell is shown in the Fig. 3b. These results exhibit good switching and reproducible behaviors with chopped visible light illumination, where the response time (including both the rising and decay time) was found to be nearly at 80 milliseconds. All the SnSe$_2$/FTO samples produce positive photocurrent with the magnitude of the generated current increasing gradually with increasing the applied potential (Fig. 3b), and hence the SnSe$_2$ belong to an n-type semiconductor.[21] The immediate rise of photocurrent from OFF to ON state proves that such SnSe$_2$ nanoflake-based photoanode is very sensitive to the visible light illumination. This is because the SnSe$_2$ nanoflake with a small bandgap is able to effectively absorb the visible light. It is worth noting that the overshooting behavior of the photocurrent can be clearly observed when switching on the light. This may be attributed to the accumulation of photogenerated electrons at the SnSe$_2$ nanoflake–electrolyte interface, which subsequently recombine with holes until a steady photocurrent is reached.

To further demonstrate the conversion efficiency of light, especially in the visible lights region, the transient current under chopped illumination of light for SnSe$_2$/FTO PEC at 0 V bias across the cell was measured under the chopped illumination of light with a wavelength ranging from 350 nm to 700 nm with a step of 10 nm. Fig. 4a–c show that the photocurrent can be reproducibly switched between "ON" state and "OFF" state by periodically turn the light on and off, which indicates fast photoresponse characteristics as well as wide spectrum responses in the visible light region. The decay of photocurrent in a continuous running is negligible, demonstrating that the SnSe$_2$ nanoflakes as photoanodes are relatively stable in the photo-oxidation process. Moreover, the relative low dark current ($\sim$10 nA) and high photocurrent ($\sim$70 nA) also guarantee an outstanding optical switching performance.

IPCE is a key parameter to evaluate the quantum yield photocurrent efficiencies, and IPCE is defined as the incident-photon-to-current-efficiency:

$$\text{IPCE} = \frac{hc}{\lambda e}\left[\frac{I_s}{P}\right] \tag{1}$$

where h is Planck's constant, c is the speed of light, λ is the wavelength of irradiation light, e is the elemental charge, I_s is the photocurrent density and P is the measured irradiance. The steady photocurrent determined from the transient current curves were used to calculate the IPCE. The IPCE spectrum for the SnSe$_2$/FTO photoanode with the wavelength in the range of 350–700 nm at the potential of 0 V $vs.$ Ag/AgCl are presented by the red line in Fig. 4d, exhibiting a broadband photoresponse. The maximum IPCE value of 3.7% was obtained at 350 nm illumination. Note that the conversion efficiency increases with the increasing photon energy in general, matching well with the absorbance spectrum as shown by the blue line in Fig. 4b. The similar trend confirms the anodic photocurrent generated from the light absorption of SnSe$_2$ nanoflakes. The visible light conversion efficiency ranging from 1% to 3.7% at 0 V is much better than that the values reported on MoS$_2$,[20] WSe$_2$,[2] and BiVO$_4$ (ref. 27) (at 0 V external potential across the cell), implying an efficient separation and transport of photo-generated charge carriers in the SnSe$_2$/electrolyte interface. The greatly enhanced PEC response of the tilted SnSe$_2$ nanoflakes could be ascribed to the high density of exposed edges, which are known as electrocatalytically active sites at the semiconductor/electrolyte interface.[28,29] In addition, the tilted structure also exposes a large surface area for the optical absorption.

The photocurrent generation process in a PEC results from charge carrier generation, separation and recombination at the semiconductor–electrolyte interface. A space charge layer is usually built when the solid semiconductor in contact with a liquid electrolyte since their initial chemical potential of electrons is different (Fig. 5a). The chemical potential of the semiconductor is determined by the Fermi level while the chemical potential is identified as the redox potential of the redox couples
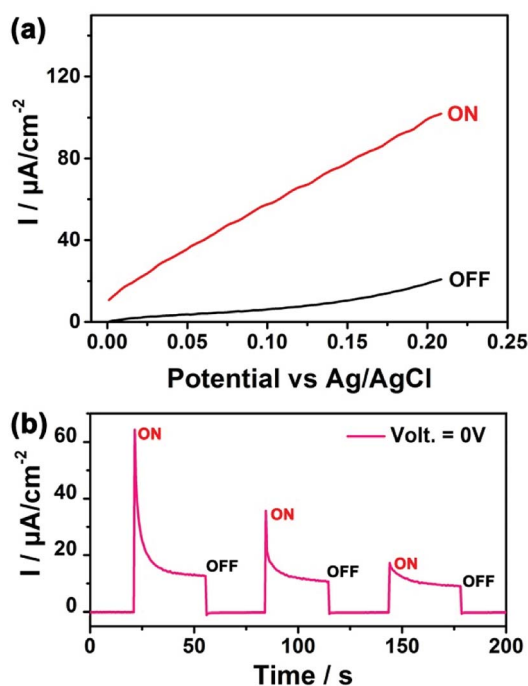

Fig. 3 (a) Linear sweep voltammograms of SnSe$_2$/FTO electrode in dark and under illumination at the applied voltage between 0 V and 0.2 V $versus$ Ag/AgCl electrode. (b) A typical current–time curve at 0 V $versus$ Ag/AgCl electrode.
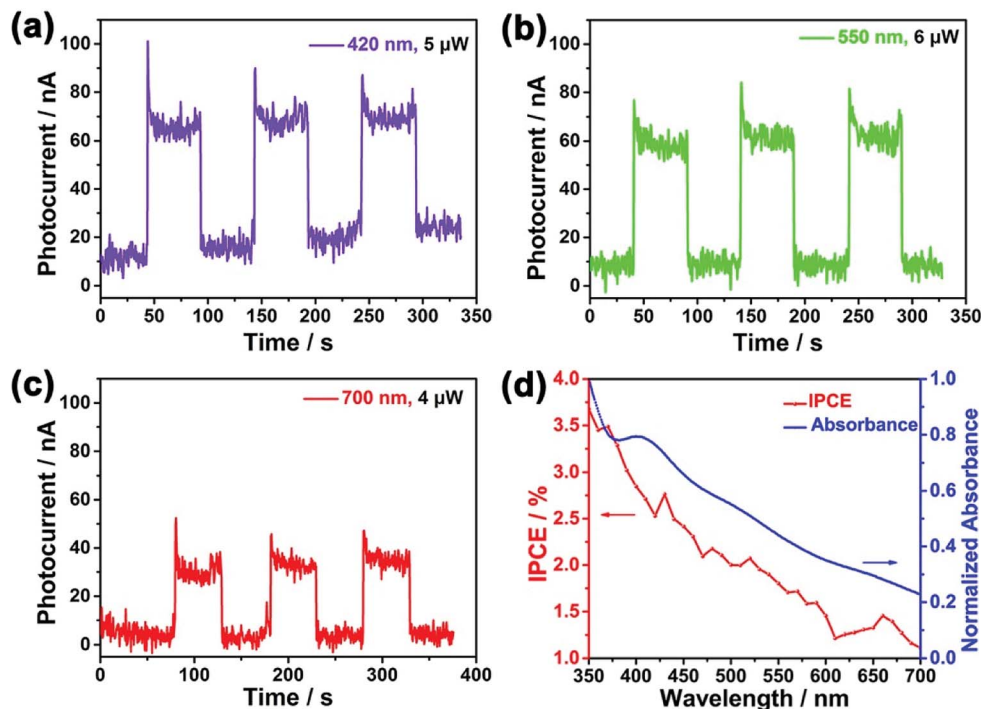
Fig. 4 Time–dependent photoresponse of $SnSe_2$ PEC under the illumination of selected wavelengths at the potential of 0 V $vs.$ Ag/AgCl: (a) 700 nm, 4 µW; (b) 550 nm, 6 µW; (c) 420 nm, 5 µW. (d) Plot of IPCE spectrum (red line) and absorbance spectrum (blue line) $versus$ wavelength at the potential of 0 V $vs.$ Ag/AgCl electrode.

for the electrolyte. In the case of n-type $SnSe_2$ thin films contacted with 0.5 M Na_2SO_4 aqueous solution, which gives an equilibrium potential at about 0.33 V $vs.$ NHE. The proximity to the OER redox potential gives a similar degree of band bending at the $SnSe_2$ thin film/electrolyte interface. Fig. 5b shows the schematic energy band diagram for $SnSe_2$ photoanode in contact with the SO_4^{2-}/SO_3^{2-} redox couple in the dark. Upon the illumination of PEC, the photo-generated charge carriers at the $SnSe_2$/electrolyte interface are separated by the electric field present in the space charge layer, as shown in Fig. 5c. Alternatively, the Pt counter electrode (CE) is aligned with the reversible redox level, while in the $SnSe_2$ electrode the quasi Fermi level splits into electron Fermi level and hole Fermi level upon the illumination. The hole Fermi level again aligns with the redox couple, leading to the reduction open circuit potential (OCP) observed in the experiments. In photoelectrocatalysis, the greater the band-bending the faster the electron/hole separation occurs, and thus the recombination of charges is therefore minimized.[30,31] Meanwhile, the $SnSe_2$/FTO interface also helps in separating charge carriers by forming a p-type Schottky barrier (by knowing the work function, $\phi_{SnSe_2} = 5.3$ eV and $\phi_{FTO} = 4.4$ eV),[32,33] retarding the recombination effect and extending the charge carrier lifetime, leading to an excellent photoresponse.

In conclusion, a simple and scalable CVD method was developed to grow tilted $SnSe_2$ nanoflakes on FTO substrates. The $SnSe_2$ with a suitable bandgap of ~1.64 eV is an idea material for PEC applications in visible light range. The unique vertically oriented morphology further endows abundant semiconductor/electrolyte interfaces and catalytic edge sites.

The robust connection between $SnSe_2$ and FTO substrates also speeds up charge transportation in the $SnSe_2$/FTO photoanode. This method is versatile and possible for scalable synthesis of other photoactive materials with this unique structure on conducting substrates.

Experimental section

Chemical vapor deposition of $SnSe_2$ nanoflakes on FTO glass

A thermal furnace equipped with fused quartz tube was employed for growing $SnSe_2$ nanoflakes on FTO glass. For a typical growth, ~50 mg Se shot (99.999+%, Alfa Aesar) was loaded in the low temperature upstream (~250 °C). ~10 mg SnSe (99.995+%, Sigma-Aldrich) was loaded in an alumina crucible at the center of the quartz tube. Cleaned FTO glass with a size of ~1.5 × 2.0 cm² was put at low-temperature downstream (~300–350 °C) for growing $SnSe_2$ nanoflakes. The tube furnace was first flushed with 500 sccm Ar for 10 min. Then, the Ar flow rate was tuned to 25 sccm. The chamber pressure was pumped down to ~1 torr to facilitate the sublimation of SnSe at 550 °C. The tube furnace was heated up with a ramping rate of 20 °C min^{-1} to 550 °C and the growth was held at 550 °C for ~5 min. Finally, the furnace was cooled down to room temperature in Ar.

TEM sample preparation

The $SnSe_2$ nanoflakes were scratched from the FTO glass using blade. Then, the $SnSe_2$ nanoflakes were dispersed in a drop of
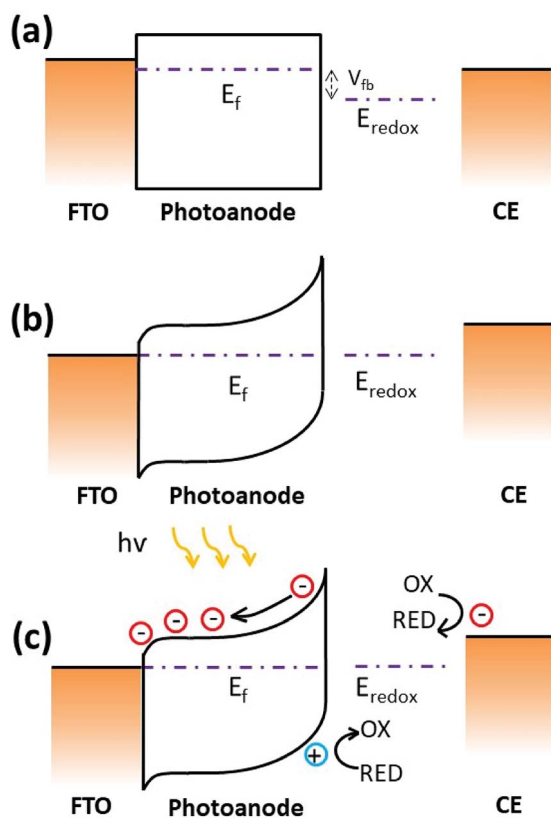
Fig. 5 Schematic energy band diagrams for flat band potential (a), and for $SnSe_2$ photoanode in contact with the SO_4^{2-}/SO_3^{2-} redox couple in the dark (b) and under illumination (c). E_f is the Fermi level energy. E_{redox} is the redox potential in the electrolyte (0.5 M Na_2SO_4). The counter electrode is Pt mesh.

ethanol directly on the FTO glass. Copper grid with porous carbon film was immersed in the $SnSe_2$/ethanol solution to capture the $SnSe_2$ nanoflakes.

Characterization of $SnSe_2$ nanoflakes

The morphology, microstructure, and chemical composition of the $SnSe_2$ nanoflakes were studied using scanning electron microscope (SEM, FEI Verios 460), transmission electron microscope (TEM, JEOL 3100FEF, 300 KeV), and X-ray powder diffraction (XRD, Philips X'Pert MPD). Raman spectra were obtained with a laser confocal microscope (NT-MDT, NTEGR Spectra) in back scattering geometry with 532 nm excitation laser.

Photoelectrochemical test of $SnSe_2$/FTO electrodes

Photoelectrochemical tests were carried out in an in-house built three-electrode cell fitted with fused silica windows at room temperature. A 250 W Xenon lamp and CM110 1/8 meter monochromator were used to illuminate the $SnSe_2$/FTO electrodes. The exposed area for light irradiation is a circle with a diameter of 1 cm. All the currents were recorded by a program controlled Potentiostat, and all the measurements were conducted against an Ag/AgCl/1 M KCl reference electrode with a Pt mesh counter electrode. 0.5 M Na_2SO_4 aqueous solution was

used as the electrolyte. The power intensity of individual wavelengths ranging from 350–700 nm was measured by a Thorlabs power meter.

Conflicts of interest

The authors declare no competing financial interest.

Acknowledgements

References

1 A. Kargar, K. Sun, Y. Jing, C. Choi, H. Jeong, Y. Zhou, K. Madsen, P. Naughton, S. Jin and G. Y. Jung, *Nano Lett.*, 2013, **13**, 3017–3022.

2 X. Yu, M. S. Prévot, N. Guijarro and K. Sivula, *Nat. Commun.*, 2015, **6**, 7596.

3 X. Xu, J. Hu, Z. Yin and C. Xu, *ACS Appl. Mater. Interfaces*, 2014, **6**, 5983–5987.

4 H. Tributsch and J. C. Bennett, *J. Electroanal. Chem. Interfacial Electrochem.*, 1977, **81**, 97–111.

5 F. R. F. Fan, H. S. White, B. L. Wheeler and A. J. Bard, *J. Am. Chem. Soc.*, 1980, **102**, 5142–5148.

6 S. Z. Butler, S. M. Hollen, L. Cao, Y. Cui, J. A. Gupta, H. R. Gutierrez, T. F. Heinz, S. S. Hong, J. Huang, A. F. Ismach, E. Johnston-Halperin, M. Kuno, V. V. Plashnitsa, R. D. Robinson, R. S. Ruoff, S. Salahuddin, J. Shan, L. Shi, M. G. Spencer, M. Terrones, W. Windl and J. E. Goldberger, *ACS Nano*, 2013, **7**, 2898–2926.

7 W. J. Zhao, R. M. Ribeiro and G. Eda, *Acc. Chem. Res.*, 2015, **48**, 91–99.

8 G. Kline, K. K. Kam, R. Ziegler and B. Parkinson, *Sol. Energy Mater.*, 1982, **6**, 337–350.

9 J. Gobrecht, H. Tributsch and H. Gerischer, *J. Electrochem. Soc.*, 1978, **125**, 2085–2086.

10 G. Kline, K. Kam, D. Canfield and B. Parkinson, *Sol. Energy Mater.*, 1981, **4**, 301–308.

11 R. Audas and J. Irwin, *J. Appl. Phys.*, 1981, **52**, 6954–6960.

12 R. Tenne and A. Wold, *Appl. Phys. Lett.*, 1985, **47**, 707–709.

13 Q. H. Wang, K. Kalantar-Zadeh, A. Kis, J. N. Coleman and M. S. Strano, *Nat. Nanotechnol.*, 2012, **7**, 699–712.

14 Y. Huang, K. Xu, Z. Wang, T. A. Shifa, Q. Wang, F. Wang, C. Jiang and J. He, *Nanoscale*, 2015, **7**, 17375–17380.

15 Z. Zeng, Z. Yin, X. Huang, H. Li, Q. He, G. Lu, F. Boey and H. Zhang, *Angew. Chem., Int. Ed.*, 2011, **50**, 11093–11097.

16 N. D. Boscher, C. J. Carmalt, R. G. Palgrave and I. P. Parkin, *Thin Solid Films*, 2008, **516**, 4750–4757.

17 V. Nicolosi, M. Chhowalla, M. G. Kanatzidis, M. S. Strano and J. N. Coleman, *Science*, 2013, **340**, 1226419.

18 G. Cunningham, M. Lotya, C. S. Cucinotta, S. Sanvito, S. D. Bergin, R. Menzel, M. S. Shaffer and J. N. Coleman, *ACS Nano*, 2012, **6**, 3468–3480.

19 U. Halim, C. R. Zheng, Y. Chen, Z. Lin, S. Jiang, R. Cheng, Y. Huang and X. Duan, *Nat. Commun.*, 2013, **4**, 2213–2219.

20 L. A. King, W. Zhao, M. Chhowalla, D. J. Riley and G. Eda, *J. Mater. Chem. A*, 2013, **1**, 8935–8941.

21 Z. Fang, S. Hao, L. Long, H. Fang, T. Qiang and Y. Song, *CrystEngComm*, 2014, **16**, 2404–2410.

22 X. Dai, Z. Li, K. Du, H. Sun, Y. Yang, X. Zhang, X. Ma and J. Wang, *Electrochim. Acta*, 2015, **171**, 72–80.

23 D. Martínez-Escobar, M. Ramachandran, A. Sánchez-Juárez and J. S. N. Rios, *Thin Solid Films*, 2013, **535**, 390–393.

24 L. Huang, Y. Yu, C. Li and L. Cao, *J. Phys. Chem. C*, 2013, **117**, 6469–6475.

25 S. Li, Y. Luo, W. Lv, W. Yu, S. Wu, P. Hou, Q. Yang, Q. Meng, C. Liu and H. M. Cheng, *Adv. Energy Mater.*, 2011, **1**, 486–490.

26 E. Trifonova, Y. I. Yanchev, P. Manou, K. Kambas and N. A. Anagnostopoulos, *J. Mater. Sci.*, 1996, **31**, 3647–3649.

27 Y. H. Ng, A. Iwase, A. Kudo and R. Amal, *J. Phys. Chem. Lett.*, 2010, **1**, 2607–2612.

28 T. F. Jaramillo, K. P. Jørgensen, J. Bonde, J. H. Nielsen, S. Horch and I. Chorkendorff, *Science*, 2007, **317**, 100–102.

29 J. Kibsgaard, Z. Chen, B. N. Reinecke and T. F. Jaramillo, *Nat. Mater.*, 2012, **11**, 963–969.

30 A. L. Linsebigler, G. Lu and J. T. Yates Jr, *Chem. Rev.*, 1995, **95**, 735–758.

31 G. G. Bessegato, J. C. Cardoso, B. F. da Silva and M. V. B. Zanoni, *J. Photochem. Photobiol., A*, 2014, **276**, 96–103.

32 T. Shimada, F. S. Ohuchi and B. A. Parkinson, *Jpn. J. Appl. Phys.*, 1994, **33**, 2696–2698.

33 A. Andersson, N. Johansson, P. Broms, N. Yu, D. Lupo and W. R. Salaneck, *Adv. Mater.*, 1998, **10**, 859–863.